Effect of Solutionizing Heat Treatment on Microstructure and Mechanical Behavior of Additively Manufactured Medium Gamma Prime Nickel Superalloy

Colleen Hilla[1], Andrew Wessman[2], Ron Aman[3], Michael Eff[3], Robert Hayes[4], Ben DiMarco[1], Edward Herderik[1], Wei Zhang[1], Michael Mills[1]

[1]The Ohio State University, Columbus, OH, 43210

[2]University of Arizona, Tucson, AZ, 85721

[3]Edison Welding Institute, Columbus, OH, 43221

[4]Metals Technology Inc., Northridge, CA, 91324

Corresponding Author:

Michael Mills

Mills.108@osu.edu

Abstract

Additive manufacturing (AM) of γ' strengthened Ni-based superalloys is appealing for use in fabrication of high temperature structural components. As AM produces unique microstructures and mechanical behaviors, a better understanding of microstructure development during post-printing heat treatment is important. An extensive set of experimental data of Rene65 printed by powder bed fusion-laser beam is reported. Effects of heat treatment on microstructure are characterized by scanning electron microscopy and electron backscattered diffraction. Elevated temperature tensile testing, tension creep, and compression creep are conducted with samples loaded parallel and transverse to the build direction. Recrystallization occurs, resulting in an equiaxed grain structure, only with supersolvus heat treatments. There is no effect of supersolvus hold time on grain growth, a behavior different from that of wrought Rene65. Subsolvus heat treatments result in a coarse bimodal precipitate structure, while rapid cooling from supersolvus results in a fine homogenous structure. Comparable tensile behavior is seen regardless of heat treatment, apart from differences in elongation to failure due to loading direction. Creep behavior is improved with supersolvus heat treatment, although increased hold time has a detrimental effect. Based on the experimental results, the relation of microstructures to mechanical behaviors for additively manufactured Rene65 is discussed.

Keywords

Nickel based superalloys; powder bed fusion; laser beam; heat treatments; texture; precipitates; gamma prime; creep

1. Introduction

Rene65 is a gamma prime (γ') strengthened nickel-based alloy originally designed for turbine rotating parts as a cast/wrought alternative to powder metallurgy alloys. As a medium γ' nickel superalloy with up to 40 vol% γ', it has superior high temperature strength and creep performance to other nickel alloys such as Nickel Alloy 718. [1-2] Cast/wrought Rene65 is characterized by a multimodal precipitate structure and fine grain size. [1-2] Traditionally, it is heat treated using a two-step heat treatment process. The first step is a subsolvus solutionizing treatment at 1066°C for 1 hour. [2] A subsolvus treatment is required for the cast/wrought alloy to avoid rapid grain growth in the supersolvus condition. This is because while increased grain sizes from supersolvus heat treatment may have mild benefit on the creep performance, the deleterious effect of larger grains on strength outweighs this benefit. The second step is an aging process at 760°C for 8 hours, which results in the formation of a fully developed precipitate structure. [2]

Powder Bed Fusion-Laser Beam (PBF-LB) is an additive manufacturing process which utilizes a powder bed and a high energy density laser source to selectively melt each powder layer. [3] It is utilized to print complex geometries and internal features not feasible through traditional manufacturing. The ability to create lighter weight parts and the ability to produce one-off parts more cost-effectively make PBF-LB a competitive process in manufacturing turbine discs made of nickel superalloys such as Rene65. However, for successful implementation of these parts, an improved understanding of the microstructure developed during printing and post-processing is needed. [4-7] PBF-LB produces microstructures that differ from traditional manufacturing methods due to a unique thermal history characterized by a series of localized, rapid heating, melting, solidification, cooling, reheating and re-cooling cycles. [5] The thermal cycles during PBF-LB effect the development of the microstructure and texture. PBF-LB builds are frequently characterized by long columnar grains parallel to the build direction (BD) as well as fine primary dendrite arm spacing owing to a combination of high temperature gradient and high solidification velocity. [8]

Various microstructural features including texture, grain structure, precipitate structure and dislocation structure effect an additively manufactured (AM'ed) material's mechanical properties especially the creep behavior. Much of the data available for creep behavior of AM'ed nickel-based superalloys is for Inconel® IN718 or IN625. [9-24] There have been only a small number of studies aiming at understanding the creep behavior of medium to high γ' alloys, and much of such work is on Alloy 738. [25-26]

The available creep data for AM'ed nickel-based alloys is split among electron beam melting, laser powder bed fusion, and direct energy deposition. [11-17, 22, 25] These printing methods produce various microstructures with varying effects on creep behavior. The general results are mixed among those that observe inferior creep behavior in AM compared to the wrought alloy, those that see similar behavior to wrought, and those that observe superior behavior to wrought. [9-17, 19, 21-24] These mixed results lead to a need for better understanding of the factors that are impacting the creep performance. There seems to be a correlation between creep behavior and processing conditions. In cases where AM had a better creep behavior than wrought, it is often attributed to sub-grain structures which are strongly affected by processing parameters. [9,15,26] Additionally, McLouth et al. showed that the use of a defocused beam improved the creep behavior of IN718 which was correlated to increased grain size and different precipitate orientation. [12] There is also some evidence that the percentage of overlap between beam passes may have an effect on the creep behavior due to detrimental grain structures that can form with certain beam overlaps. [18]

Post printing heat treatments play a major role in creep behavior. [9-11,13,18,21-22] For example, some studies have reported benefits of solutionizing and aging of IN718, while other studies have shown additional improvement can be obtained with direct aging of IN718 or homogenization and aging. [10-11,13,18]

It is also important to take into consideration the loading direction of the test in relation to the build direction. [9,17-18,25] Generally, improved creep behavior is observed when loading parallel to the build direction than loading transversely, attributed to differences in grain size and texture. Columnar grains lead to a larger effective grain size parallel to the build direction which improves creep behavior. [12] There may also be a preference of <001> grains parallel to the build direction, for which there is evidence of improved creep behavior. [25] Reduced creep ductility due to grain boundary decohesion and intergranular cracking are seen when loading transversely or perpendicularly to the build direction for many AM'ed samples. [24-26]

A better understanding of the effect of processing on creep behavior is needed across all alloy systems particularly for medium to high volume fraction γ' nickel alloys where there is minimal data available. The aim of this study is to provide a comprehensive set of experimental data on the effect of variations in heat treatment on texture, precipitates and creep behaviors (i.e., tension vs compression) in Rene65 printed by PBF-LB. Moreover, the relation of microstructures to mechanical behaviors is discussed for the AM'ed Rene65.

2. Material and Processing

Gas atomized Rene65 powder with a particle size in the range of 15 to 45 μm was used, and the powder chemical composition is shown in Table I.

Table I: Rene65 powder composition

	Ni	Co	Cr	Ti	Al	Mo	W	Fe	Nb	Zr	B	C
Wt%	Bal.	13	16	3.7	2.1	4	4	1	0.7	0.05	0.016	0

Mechanical and microstructure test specimens were printed on a Concept Laser M2 Series 3 machine. A spot size of 120 µm, a power of 200 W, a hatch spacing of 90 µm, and a travel speed of 1000 mm/s were used for all samples. For printing, a hatch-strip scan strategy with 10mm strip lengths and 90° hatch rotations between layers was employed.

Samples were post-processed in a two-step heat treatment process. In the first step, samples were solutionized at varying temperatures, times, and cooling rates, as shown in Table II. For better temperature control, the heating process was divided into three segments: 100°C/min until 1000°C, then 20°C/min up to 10°C below target temperature, and finally 10°C/min until target temperature. Solutionizing temperatures of 1066°C, 1100°C, 1150°C, and 1200°C were used with a standard hold time of 1 hour and a cooling rate of 200°C /min. Note that the solvus temperature for Rene65 is 1111°C. [36] The subsolvus heat treatment used in this study mimics the heat treatment optimized for the wrought alloy. Longer hold times of 4 and 8 hours were also used for the supersolvus temperature of 1150°C. Shorter hold times of 15 and 30 minutes were used for near subsolvus temperature of 1100°C. Since there is a strong dependence of creep behavior on cooling rate of the solutionizing treatment for wrought Rene65, another cooling rate was tested in this study. Specifically, a slower cooling rate of 50°C/min was used for 1066°C and 1150°C. In the second step, all solutionized samples were aged at 760°C for 8 hours.

Table II: Heat treatment conditions for solutionizing. All solutionized samples were then aged at 760°C for 8 hours.

Temperature	**Cooling Rate**	**Hold Time**				
		15 mins	30 mins	1 hour	4 hours	8 hours
1066°C	200°C /min			X		
	50°C /min			X		
1100°C	200°C /min	X	X	X		
1150°C	200°C /min			X	X	X
	50°C /min			X		
1200°C	200°C /min			X		

An FEI Apreo scanning electron microscope (SEM) was used for microstructure characterization. Specifically, grain size and structure were analyzed through electron backscatter diffraction (EBSD) at a voltage of 20 kV, a current of 26 nA and a working distance of 20 mm. The reference direction for all EBSD maps is the surface normal. Precipitate size, morphology, and distribution were imaged in backscattered electron (BSE) mode with a voltage of 5 kV, a current of 0.4 nA and a working distance of 7.5 mm. Area fraction measurements were performed using Fiji, an open-source image analysis software, where a threshold was applied to estimate the area fraction of precipitates. Thresholding was completed manually for area fraction measurements and particle size measurements. The measurements were done by analyzing different regions on the sample with a minimum of 70 particles analyzed.

Hot tension testing was done in an MTS machine. The samples were loaded in tension at 704°C until complete fracture according to ASTM E21. As shown in Table III, the materials tested included as-built, solutionized at 1066°C (subsolvus) then aged, solutionized at 1150°C (supersolvus) then aged, and heat-treated conventionally wrought material used for comparison. The AM'ed materials were also loaded both along and transverse to the build direction. Due to testing issue, the data for subsolvus loaded transversely was not successfully collected, and this test was not repeated due to limited material availability.

Table III: Conditions used for hot tension testing. All tests were at 704°C

Material		**Testing direction to the build direction**	
		Transverse	Parallel
Wrought: Solutionized at 1066°C for 1hr and aged		N/A	
Printed by PBF-LB	As-built	X	X
	Solutionized at 1066°C for 1hr with cooling rate of 200°C /min and aged	X	X
	Solutionized at 1150°C for 1hr with cooling rate of 200°C/min and aged	X	X

Table IV summarizes the creep testing conditions. Tension creep testing was completed for wrought, as-built, subsolvus 1066°C, and supersolvus 1150°C loaded both along and transverse to the build direction. Tension creep was done at 704°C and 690 MPa, and samples were strained to 0.5% creep strain. Due to anisotropy between tension and compression creep, a higher load was utilized in the latter to better match the strain rate achieved in tension creep for the as-built condition. Specifically, compression creep tests were performed at 704°C and 950 MPa with samples loaded in both parallel and perpendicular to the build direction. To save testing time, the tests were stopped when samples were strained to 1% creep strain. Additional compression creep tests of different heat-treated samples were completed parallel to the build direction at 690 MPa for a direct comparison to the tension creep; these samples were also tested to 1% strain.

Compression creep samples were 7-mm-long blocks with square cross section of 2.8 mm × 2.8 mm and were loaded along the length side. Tension creep and tensile samples were threaded round ones with diameter of 6.35 mm and gauge length of 25 mm. All mechanical testing was completed in air.

Table IV: Conditions used for creep testing where C indicates a compression creep and T a tension creep. All tests were performed at 704°C

Load (MPa)				690		950	
Loading direction with respect to build direction				Transverse	Parallel	Transverse	Parallel
Material: Wrought				T			
Material: As-built					C, T	C	C
Material: Solutionized and aged	Temp. (°C)	Time (mins)	Cooling rate (°C /min)				
	1066	60	200		C, T	C	C
			50			C	C
	1100	15	200			C	C
		30				C	C
		60				C	C
	1150		50			C	C
		60	200		C, T	C	C
		240				C	C
		480				C	C
	1200	60	200			C	C

3. Results

3.1 Effect of Post-Processing Parameters on Microstructure

3.1.1 As-Built Microstructure

First, the as-built microstructure is briefly described which provides the basis to understand the development of the structure with varying post-processing heat treatment parameters. The as-built condition has no discernable precipitates at the length scale observed in SEM. Figure 1a shows the lack of precipitates as well as the cellular solidification structure. A directionally solidified microstructure is present, with long columnar grains parallel to the build direction (Figure 1b) and an irregular square lattice of grains observed transverse to the build direction (Figure 1c); the latter correlates with the rastered laser beam path. [6,7,27] The grain size transverse to the build direction ranges from approximately 25 to 40 μm and that parallel to the build direction ranges from approximately 40 to 80 μm. The aspect ratio ranges between 1.6 to 1.9. Texture parallel and transverse to the build direction are outlined in Figures 1 e and f respectively. A stronger <001> type texture is seen parallel to the build direction as well as a small preference for the <110> type direction. This is expected as <001> is the preferred growth direction for cubic materials. [28]

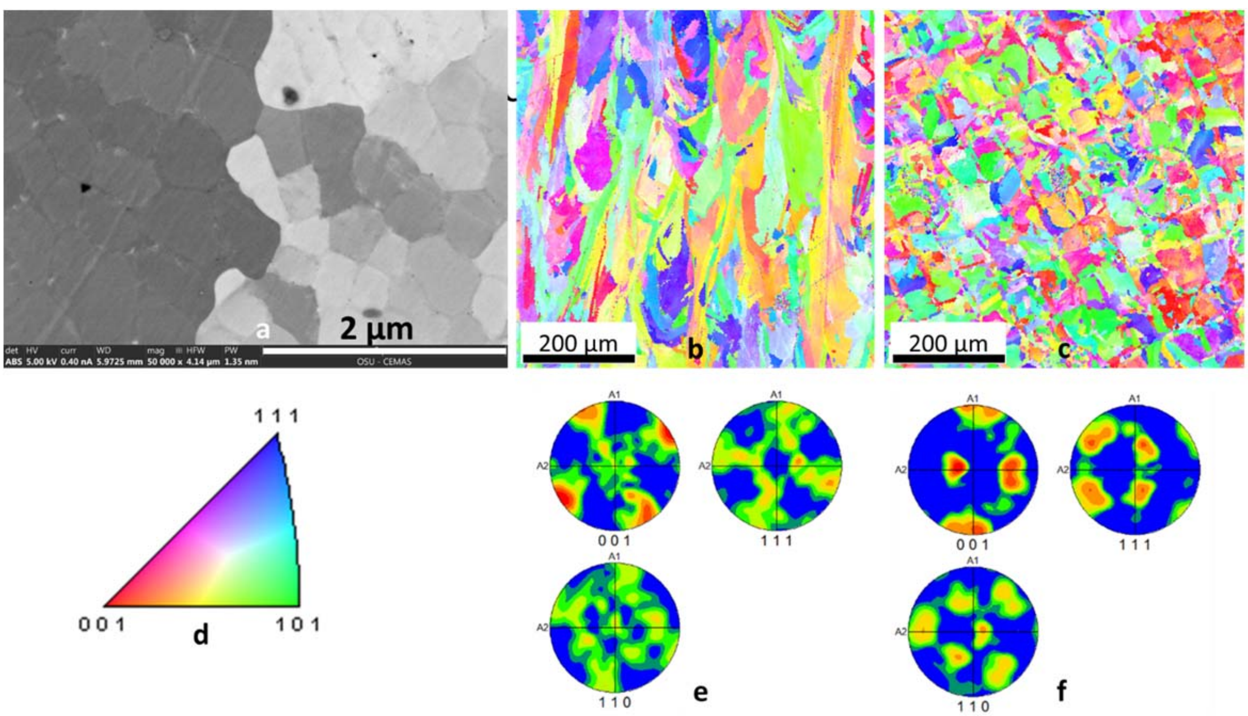

Figure 1: As-built microstructure (a) BSE image transverse to build direction, (b) grain structure based on EBSD analysis parallel to build direction (BD), and (c) grain structure based on EBSD analysis perpendicular to BD. The color correspondence to grain orientation for the inverse pole figure maps is shown in (d), texture along the build direction shown in (e), and texture transverse to build direction shown in (f)

3.1.2 Effect of Aging Heat Treatment

To characterize the precipitate evolution during heat treatment, the microstructure in the as-solutionized condition is compared to that in the solutionized and aged condition. This will form a baseline as subsequent results will show the as-aged material. As shown in Figure 2, a bimodal precipitate structure is obtained after the subsolvus heat treatment at 1066°C for 1 hour, while a fine uniform precipitate structure is obtained after the supersolvus heat treatment. Moreover, there is minimal precipitate growth due to aging in either the subsolvus or supersolvus conditions.

Specifically, for the 1066°C (subsolvus) condition with bimodal precipitate structure, prior to aging the average secondary precipitate size is 178 nm, and the average tertiary precipitate size is 28 nm. After aging the average secondary precipitate size is 167 nm, and the average tertiary precipitate size is 24 nm. Note the standard deviation of large secondary γ' was approximately 70 nm, and that of tertiary γ' was approximately 7 nm. For the 1150°C (supersolvus) condition with uniform fine precipitate structure, the average precipitate size prior to and after aging is 67 nm and 53 nm, respectively, with standard deviation of 8 nm. Given that the average grain sizes are well within the standard deviation of the measurements, aging does not have an appreciable effect on precipitate coarsening.

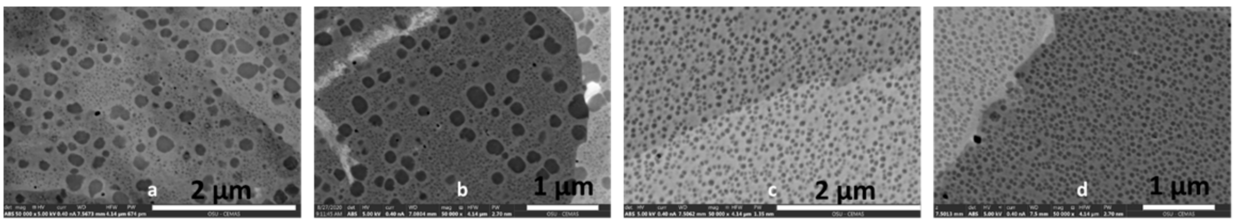

Figure 2: BSE of γ' precipitates (a) subsolvus 1066°C/1hr with no aging, (b) 1066°C/1hr and aged, (c) supersolvus 1150°C/1hr with no aging, and (d) 1150°C/1hr and aged. Cooling rate of 200°C/min used for each sample

Aging is expected to have minimal effect on grain structure as it is completed well below the solvus temperature and γ' is present in the microstructure to produce pinning. Figure 3 shows similar grain structures before and after aging for both supersolvus and subsolvus conditions.

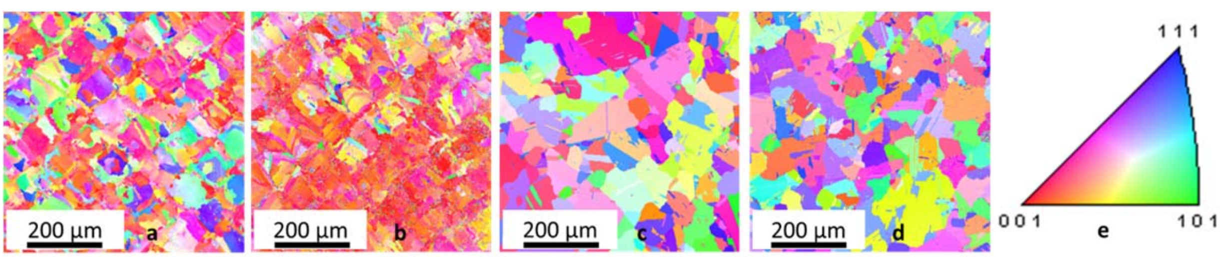

Figure 3: EBSD of grain structure transverse to BD (a) subsolvus 1066°C/1hr without aging, (b) 1066°C/1hr and aged, (c) supersolvus 1150°C/1hr without aging, and (d) 1150°C/1hr and aged. Cooling rate of 200°C/min used for each sample

3.1.3 Effect of Sub/Supersolvus Temperature

Various effects of solutionizing temperature are seen with respect to both the precipitate and grain structures. As reported earlier, a coarse bimodal precipitate structure is seen at the subsolvus solutionizing temperature of 1066°C. For ease of comparison, this microstructure is also shown in Figure 4a. For temperatures at 1100°C, 1150°C, and 1200°C, a fine homogenous precipitate structure developed, as shown in Figure 4b, c and d, respectively.

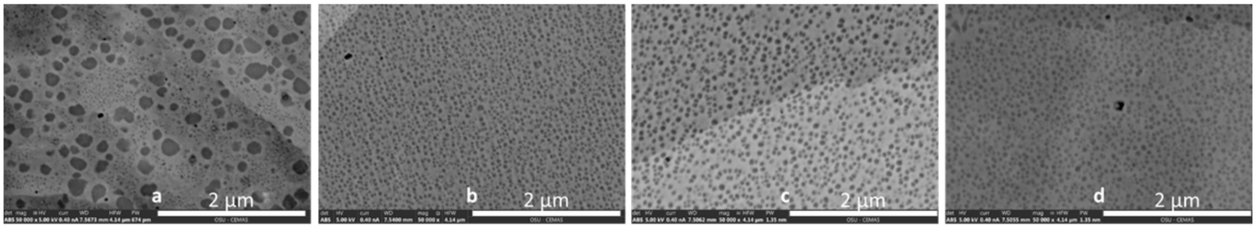

Figure 4: BSE of γ’ precipitates (a) 1066°C, (b) 1100°C, (c) 1150°C, and (d) 1200°C. Hold time of 1 hour and cooling rate of 200°C/min used for each sample

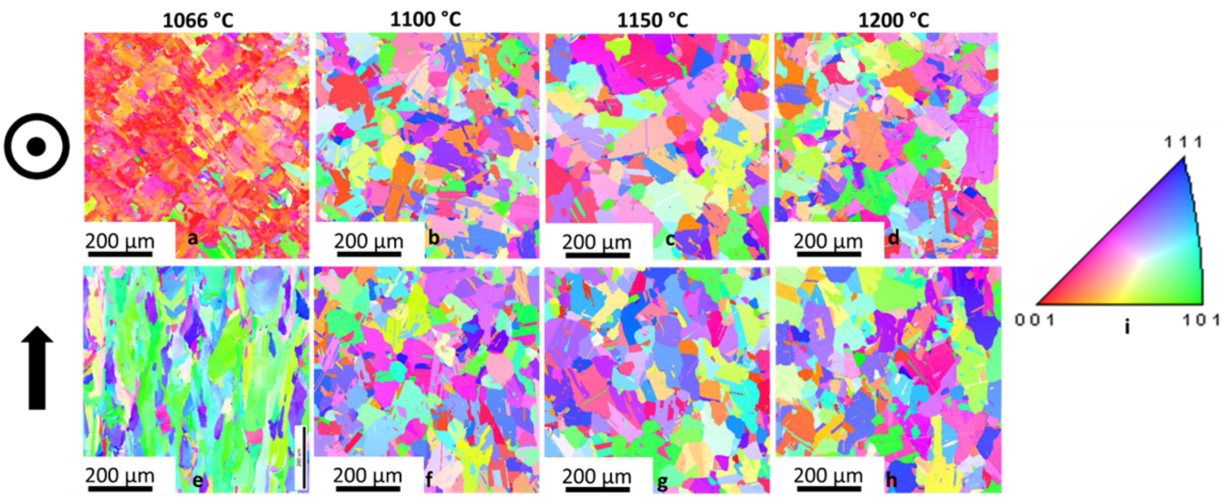

Figure 5: EBSD images showing the grain structure (a, b, c, d) transverse to BD, (e, f, g, h) parallel to BD, after hold time of 1 hour at the following temperatures (a,e) 1066°C, (b,f) 1100°C, (c,g) 1150°C, (d,h) 1200°C. Cooling rate of 200°C/min used for each sample

3.1.4 Effect of Sub/Supersolvus Hold Time

As precipitate dissolution depends on diffusion kinetics and thus time at temperature, a pronounced effect of hold time on the precipitate and grain structures is expected near and below the solvus temperature. A bimodal precipitate structure is seen with a 15-minute hold time at 1100°C, as shown in Figure 6a. Moreover, the large precipitates are located preferentially at the prior cell boundaries, which is likely due to micro-segregation of γ’ formers during rapid solidification in PBF-LB. [29] There is some evidence of these large precipitates retained at the grain boundaries for longer hold times. This can be seen for 1 hour hold time in Figure 7, which is likely due to the precipitates not fully solutionizing and continuing to pin the grain boundaries.

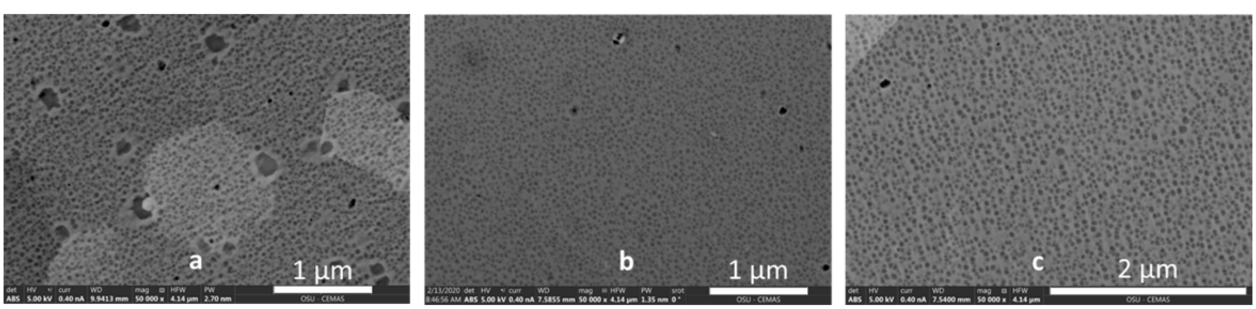

Figure 6: BSE of γ’ precipitates for heat treatments at 1100°C+ aging, cooling rate 200°/C min, and hold time (a) 15 min (b) 30 min (c) 1 hour

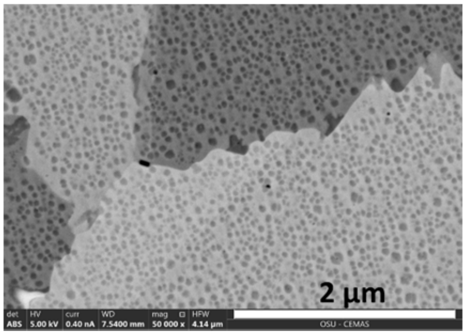

Figure 7: BSE of large precipitates retained at the grain boundaries at 1100°C/1hour hold time

The directionally solidified grain structure was maintained for the 15-minute hold time at 1100°C, as shown in Figure 8a and d. On the other hand, for longer hold times (i.e., 0.5 and 1 hr), recrystallization occurred, resulting in an equiaxed grain structure. This can be seen below in Figure 8b and e for 0.5 hr hold time, and Figure 8c and f for 1 hr hold time.

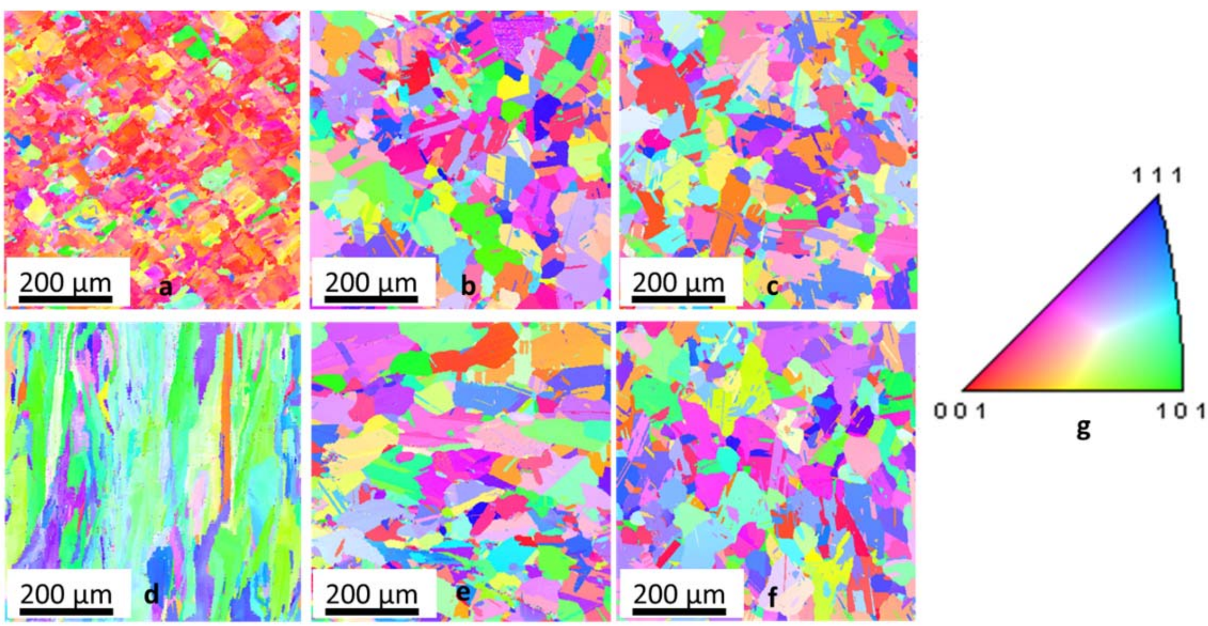

Figure 8: EBSD grain structure for heat treatments at 1100°C + aging, cooling rate 200°C/min (a) 15 min transverse to BD, (b) 30 min transverse to BD, (c) 60 min transverse to BD, (d) 15 min parallel to BD, (e) 30 min parallel to BD, and (f) 60 min parallel to BD

As shown in Table II, in addition to 1 and 4 hours, an extended hold time of up to 8 hours was performed in the supersolvus at 1150°C in an attempt to determine the “equilibrium” microstructure at this temperature. As shown in Figure 9, a fine, homogenous precipitate structure characterizes all three hold times, with some evidence of slightly coarser precipitates at longer hold time. While the homogenous structure is expected from a supersolvus heat treatment where full solutionizing is able to occur, larger precipitates may form due segregation of Ti and Al during printing leading to preferential nucleation of particles near prior cell boundaries. [29] A large second phase particle is seen with the 4 hour-hold time marked with a cross in Figure 9b. This type of particle is not unique to this heat treatment but may be more prominent with longer hold times. Due to low volume fraction of these secondary particles, further investigation such as EDS was not completed. However, the backscatter contrast suggests it likely to be a nitride, a type of particle observed in the wrought alloy.

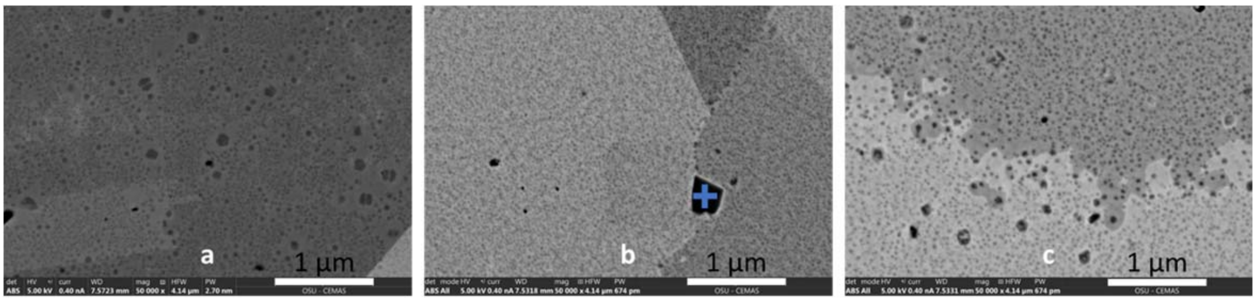

Figure 9: BSE images of γ' precipitates for heat treatments at 1150°C+ aging, cooling rate 200°C/min: (a) 1 hour hold time, (b) 4 hours hold time, and (c) 8 hour hold time.

Increasing the hold time at supersolvus condition does not lead to an increase in the grain size. This can be seen in Figure 10. The stable grain structure is not likely caused by γ' precipitate pinning as the sample was held well above the γ' solvus temperature at 1150°C.

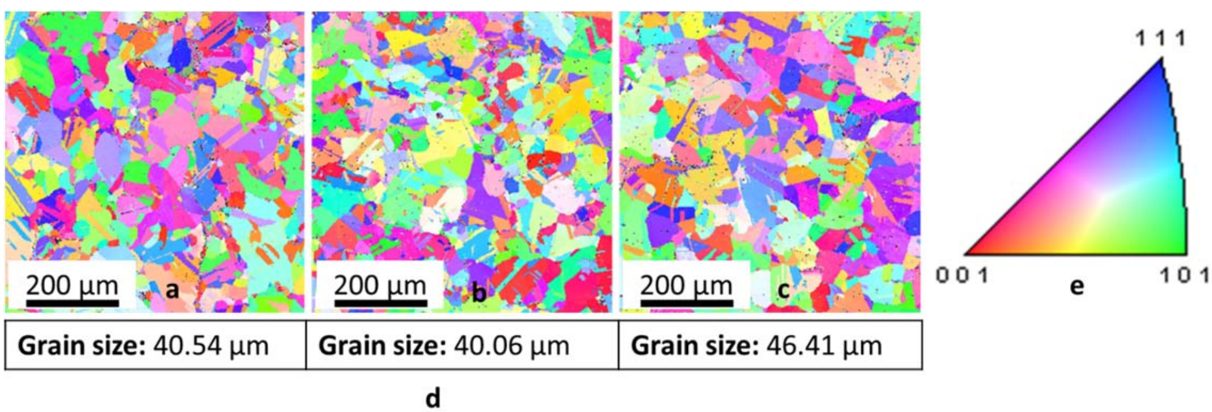

Figure 10: EBSD grain structure and grain size for heat treatments at 1150°C + aging, cooling rate 200°C/min (a) 1 hour hold time, (b) 4 hour hold time, and (c) 8 hour hold time

3.1.5 Effect of Cooling Rate

Based on data for wrought Rene65, the cooling rate after solutionization is expected to have a large impact on the precipitate structure. Following supersolvus heat treatment (1150°C), more rapid cooling rate (Figure 11a) results in a fine γ' distribution formed during cooling. Conversely, at slower cooling rate (Figure 11b), there is a large increase in the size of secondary precipitates, as well as the development of tertiary precipitates. It is noted that the measured area fraction of γ' precipitates stays consistently from 29.84% for the slower cooling rate to 31.38% for the faster cooling rate in the supersolvus condition.

In the subsolvus heat treatment (1066°C) there is a minor increase in precipitate size and small decrease in the volume fraction of tertiary γ' for the slower cooling rate, as shown in Figure 11c and d.

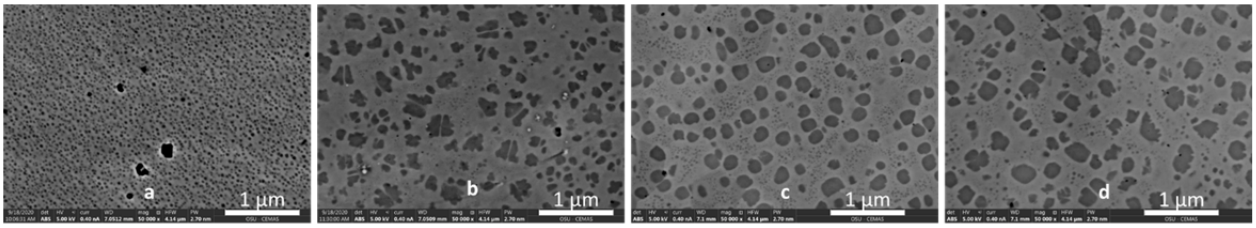

Figure 11: BSE of γ' precipitates (a) 1150°C, 100°C/min, (b) 1150°C, 50°C/min, (c) 1066°C, 100°C/min, and (d) 1066°C, 50°C/min. All samples are in the aged condition

In both the subsolvus and supersolvus conditions, there is little to no effect on the grain size or structure with different cooling rates, as shown in Figure 12.

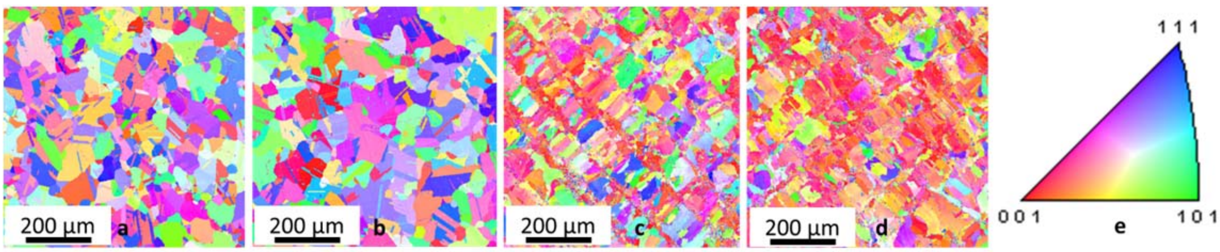

Figure 12: EBSD of grain structure imaged transverse to the BD (a) 1150°C, 100°C/min, (b) 1150°C, 50°C/min, (c) 1066°C, 100°C/min, and (d) 1066°C, 50°C/min

3.1.6 Grain Rotation Orientation Deviation

The grain rotation orientation deviation (GROD) parameter can provide insight into geometrically necessary dislocation content and stored strain energy in deformed microstructures [30]. The GROD for the as-built, subsolvus, and supersolvus are presented in Figure 13. High maximum grain rotation is seen in the as-built (Figure 13a) and subsolvus heat treated conditions (Figure 13b): 20 and 18 degrees respectively. A much lower maximum rotation of 5 degrees is seen in the supersolvus heat treated condition (Figure 13c). For a more direct comparison, Figure 13 d and e plot the relative rotation for subsolvus and supersolvus conditions on the same grey scale where lighter color indicates higher relative rotation. A significant decrease in geometrically necessary dislocation content and inferred strain energy is seen in the supersolvus condition with a recrystallized microstructure.

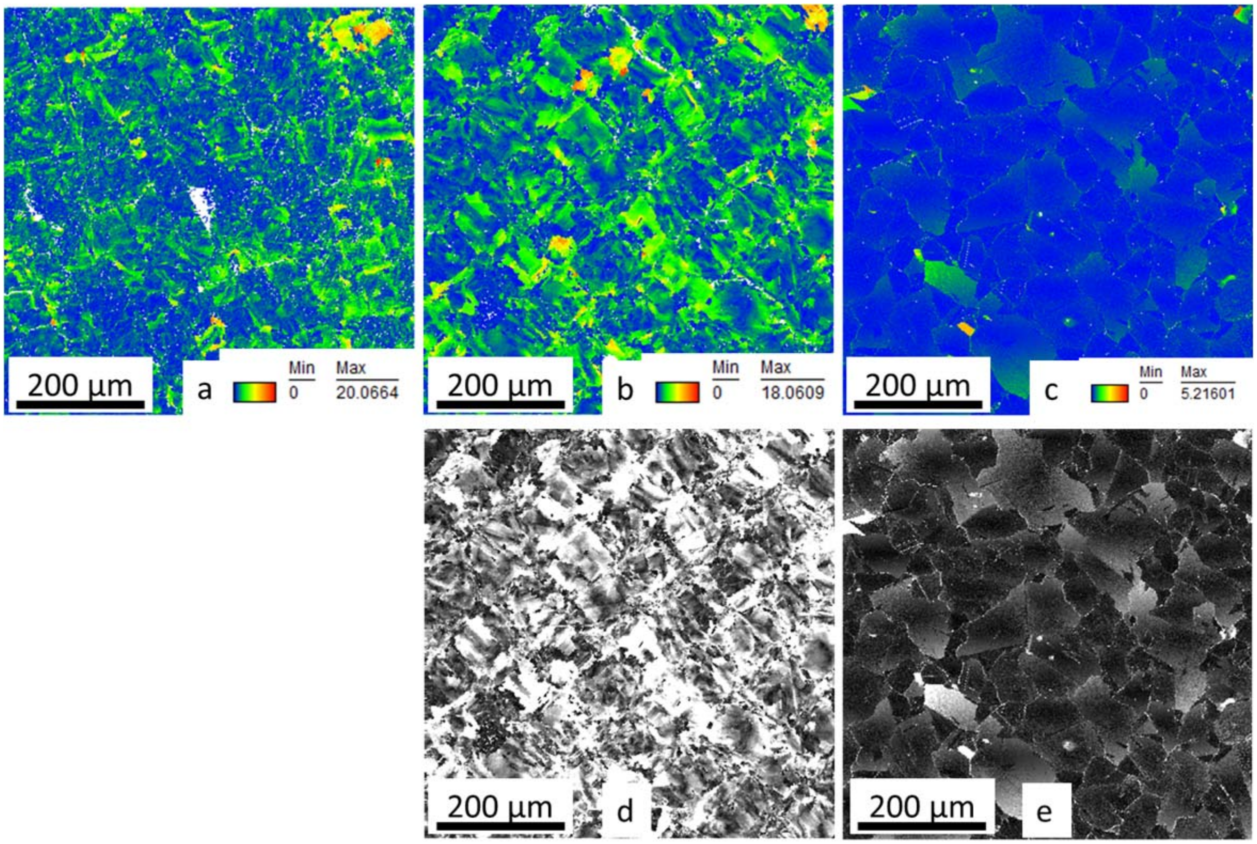

Figure 13: Grain rotation orientation deviation (a) as-built maximum rotation of 20 degrees, (b) 1066°C/1hr maximum rotation of 18 degrees, (c) 1150°C/1hr maximum rotation of 5 degrees, (d) 1066°C/1hr relative rotation, and (e) 1150°C/1hr relative rotation

3.2 Mechanical Behaviors

Microstructures formed due to various heat treatment parameters have significant impact on the mechanical behaviors of the material, as described in the following. Unless otherwise noted, supersolvus samples for mechanical testing were heat treated at 1150°C for 1 hour with a cooling rate of 200°C/min and subsolvus samples for mechanical testing treated at 1066°C for 1 hour with a cooling rate of 200°C/min. All samples for mechanical testing were aged at 760°C for 8 hours.

3.2.1 Tensile Deformation

Figure 14 shows the effect of heat treatment condition on yield strength, ultimate tensile strength (UTS) and elongation at failure when tested at 704 °C. Due to the limited sample availability, each condition was only tested once. In general, the yield and UTS of AM'ed Rene65 are lower than those of the wrought condition, especially when the AM'ed material was loaded perpendicularly to the build direction. A large discrepancy is also observed when the AM'ed material was loaded parallel versus perpendicular to the build direction. Specifically, the elongation was poor (only 1%) in the latter. Elongation was much improved when tested parallelly to the build direction with the subsolvus heat treated condition having the lowest elongation (6%) and supersolvus having the highest elongation (10%).

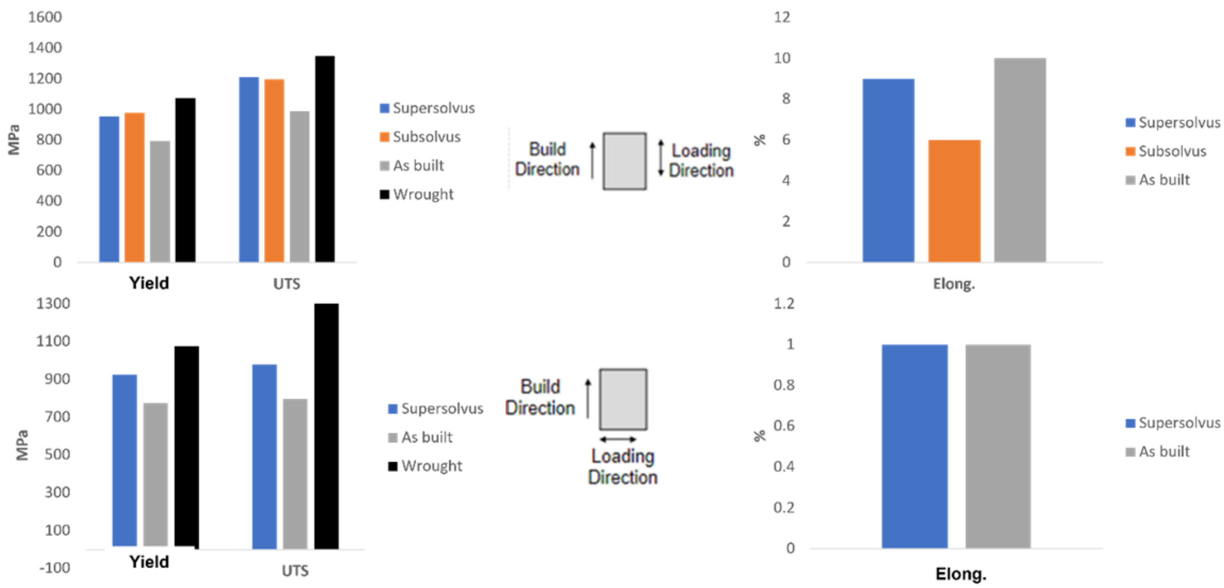

Figure 14: Tensile behavior at elevated temperature of 704°C. Wrought data taken from Ref. [36]

3.2.2 Tension and Compression Creep

As there can exist an asymmetry between tension and compression creep, it is important to understand both behaviors as many parts can be subjected to complex loading conditions. The behavior in tension creep in the subsolvus AM, supersolvus AM, as-built AM, and wrought alloy is shown in Figure 15 along with the compression creep of the matching AM conditions. It is noted that as-built and heat-treated AM'ed samples were also tension loaded perpendicular to the build direction but they all failed prematurely at low strain values. As the premature failure of these transverse-loaded samples were likely dominated by printing defects, their results are not further discussed, and all AM'ed samples in Figure 15 were loaded parallel to the build direction.

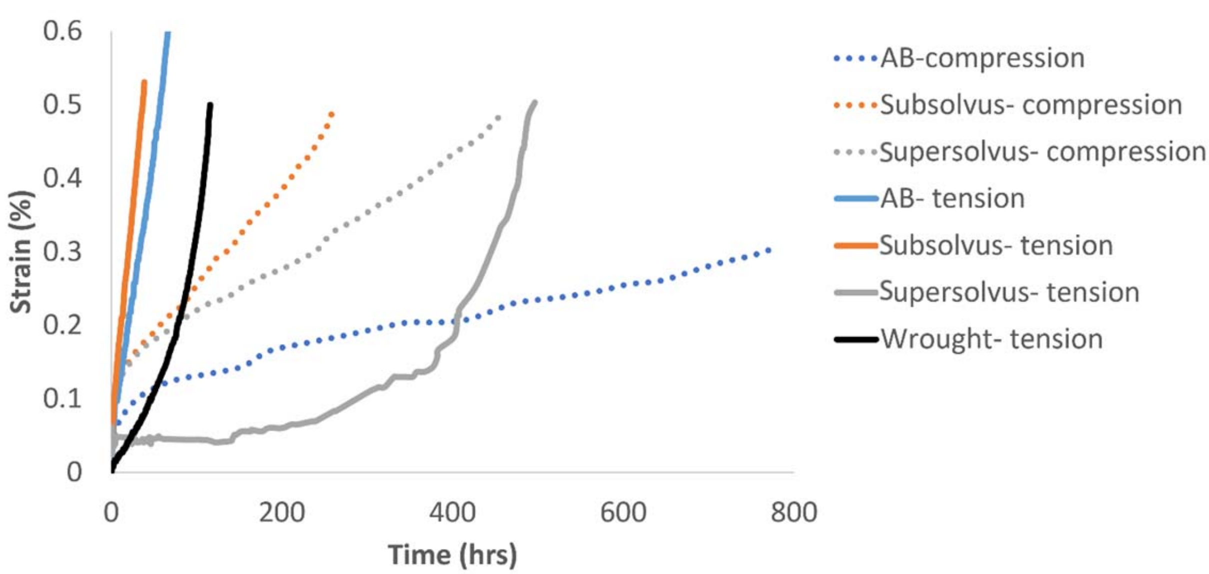

Figure 15: Tension vs compression creep behaviors at 704°C and 690 MPa. AB stands for as-built. All AM'ed samples were loaded parallel to the build direction.

3.2.3 Compression Creep at High Stress

As shown in Figure 15, the compression creep samples loaded at 690 MPa took at least 300 hours to reach just 0.5% strain. To more efficiently test samples with various heat treatments, a high stress of 950 MPa was used to test additional compression creep samples. As stated earlier, this high stress was selected to match the strain rate achieved in tension creep of the as-built sample.

A summary of the creep response (time to 1% strain) for various subsolvus and supersolvus heat treated samples loaded at the high stress of 950 MPa is shown in Figure 16. With a hold time of 1 hour, supersolvus heat treated material (1150°C) exhibits superior behavior to subsolvus (1066°C, and 1100°C) heat treated condition in compression creep. For supersolvus, an increased hold time above 30 minutes (i.e., 1 hour or higher) has a detrimental effect on the compression creep behavior. There is no clear impact of cooling rate or loading direction on compression creep behavior, as shown in Figure 16.

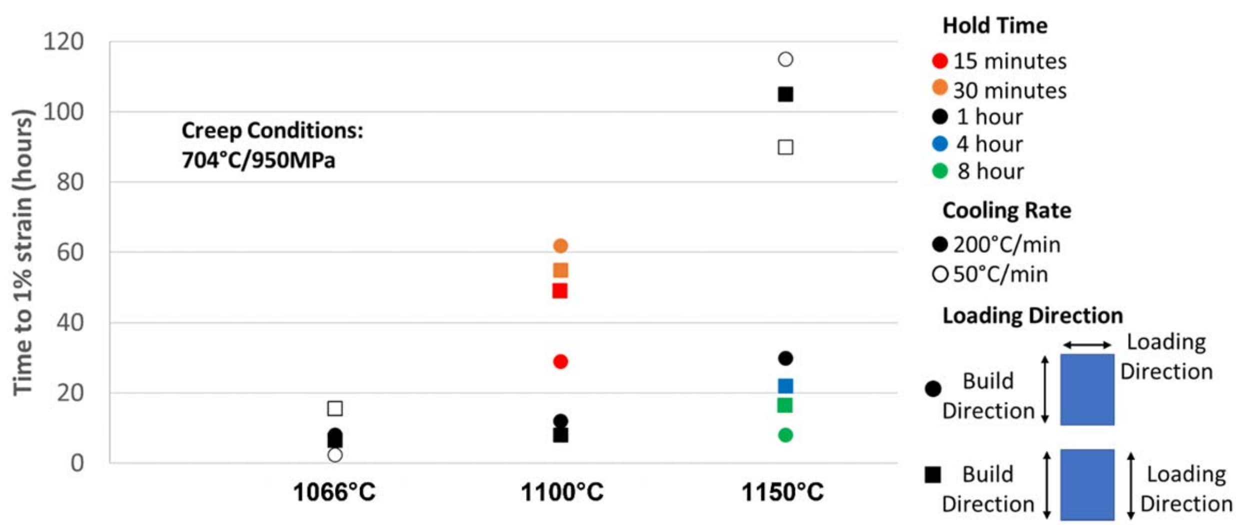

Figure 16: Compression creep time to 1% strain where color indicates hold time, opened or closed shape indicates cooling rate, and shape indicates loading direction for each sample. For example, the open black square at 1066 °C designates a sample solutionized at this temperature for 1 hour, cooled at 50 °C/min, and then aged at 760°C for 8 hours. It was tested parallelly to the build direction.

4. Discussion

4.1. Processing Effects on Microstructure

4.1.1. Precipitation

The as-built microstructure has no discernable precipitates as shown in Figure 1. This indicates that either no precipitates are present, or nanoscale precipitates are present. This question is the subject of more detailed transmission electron microscopy (TEM) investigation and will be reported elsewhere. In either case, this is due to rapid cooling common in the PBF-LB process. [31] In general, if sufficiently high cooling rates are achieved, precipitation is prevented as there is not sufficient time for the necessary diffusion for precipitation. In the case of nano-scale precipitation, nucleation is able to occur, but there is insufficient time for growth.

Upon heat treatment, there are two primary precipitate structures that are formed: a coarse bimodal precipitate structure and a fine homogenous structure seen in Figures 2, 4, 6, 9, and 11. These precipitate distributions can be explained on the basis of whether sufficient temperature and time are available for full dissolution. [32] Specifically, the precipitate development is schematically shown in Figure 17 and described in the following.

Due to capacity to form a high volume fraction of γ’, a low lattice mismatch between γ’ and γ, and segregation of γ’ forming elements to interdendritic regions, there is a large driving force for both γ’ nucleation and growth in this alloy. [33] Hence, it is anticipated γ’ precipitates quickly formed around grain boundaries and interdendritic regions when the as-built microstructure is heated up during heat treatment, as shown by the inset image 1 in Figure 17. In the case of subsolvus or short hold times near solvus, the hold temperature and/or time are insufficient to fully dissolve those γ’ precipitates formed during heating. Therefore, precipitates nucleate and coarsen at elevated temperature (as shown by 2b). [34] On the contrary, for supersolvus and long hold times near solvus, precipitates fully dissolve during the hold (as shown by 2a). On cooling with subsolvus, the precipitate coarsening is largely independent of cooling rate and tertiary γ’ develops (as shown by 3c). In supersolvus all precipitates form on cooling therefore with fast cooling precipitates have little time to coarsen (as shown by 3a). [35] However, it is noted that γ’ precipitation can involve multiple bursts during cooling. When heat treated at 1150°C (supersolvus), there is a high degree of supersaturation of γ’ formers in the γ matrix due to the full dissolution of precipitates and homogenization. Upon cooling, such supersaturation likely promoted a first burst of γ’ nucleation at relatively high temperature. Despite the fast cooling rate (200°C/min), these particles were able to coarsen, resulting in a small population of large γ’ precipitates (see Figure 9a). Upon further cooling, a second burst took place uniformly across the grains, resulting in the formation of small γ’ precipitates although nucleation was suppressed around those existing large precipitates. When heat treated at 1100°C (near solvus), the degree of supersaturation was lower compared to 1150°C, and more undercooling was thus required to nucleate γ’ precipitates. These precipitates had less time to coarsen due to sluggish diffusion kinetics at lower temperatures, resulting in homogenously dispersed fine precipitates after cooling (see Figure 6c).

Finally, there is minimal additional precipitate development during aging of the AM’ed Rene65. This differs from the wrought alloy which shows growth of the tertiary γ’ during aging. [36] The reason for this is likely due to the precipitate size on cooling. Specifically, in the subsolvus condition prior to aging, which is designed after the standard wrought treatment, the average size of tertiary γ’ is 28 nm. This is already larger than the tertiary γ’ in the wrought aged condition which has an average size under 20 nm. [36] One hypothesis for tertiary γ’ precipitates in AM’ed material being larger than those in the wrought material is the fine dendritic structure and consequently shorter diffusion distance that facilitates γ’ growth in the former. Further investigation into this mechanism is required. The above results indicate aging process may not be necessary for processing of AM’ed Rene65 which will reduce processing time.

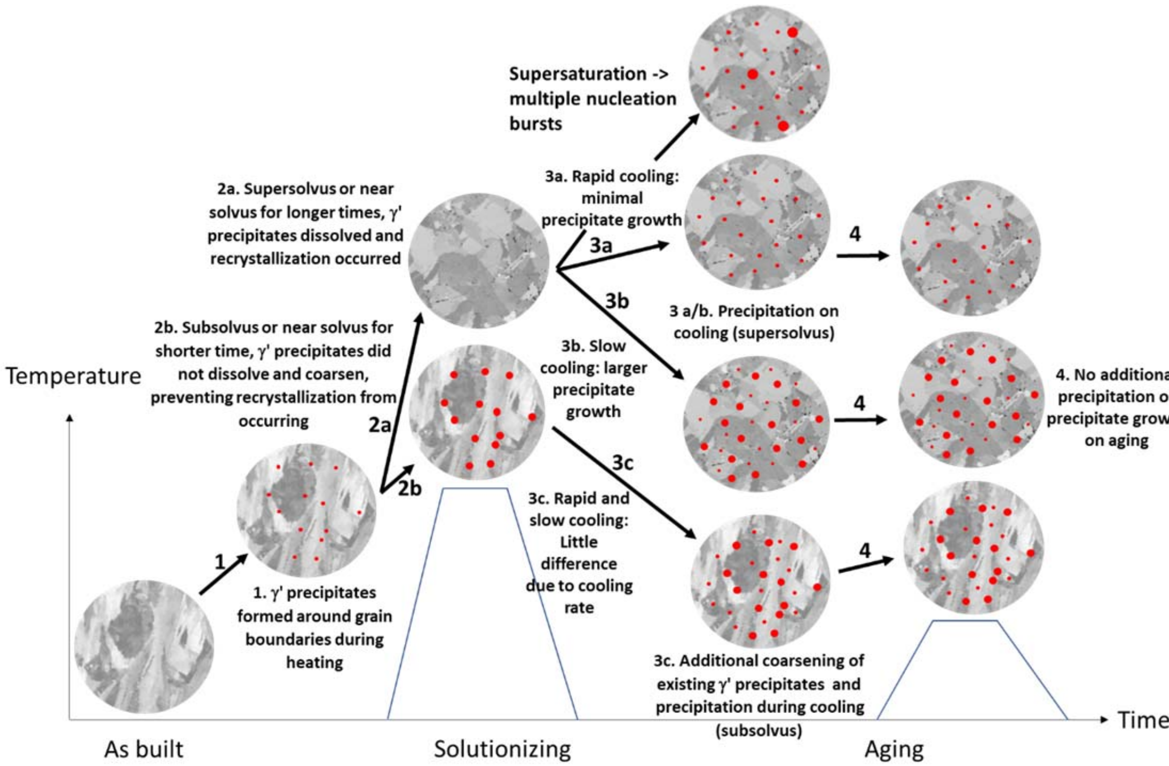

Figure 17: Schematic plot showing precipitate development through heat treatment process where supersolvus temperature is 1150 °C, near solvus is 1100 °C and subsolvus is 1066 °C

4.1.2. Recrystallization

Due to rapid cooling and extensive micro-segregation, the formation of non-equilibrium microstructures is common in AM'ed materials. [37-38] Segregation has been shown to affect diffusion and recrystallization behavior in various materials. [39-41] Additionally, extensive thermal cycling occurs during additive manufacturing, leading to a large accumulation of residual stress/strain. Coupling these factors leads to a high driving force for recrystallization. [42] This can be seen with the change in grain rotation and stored strain energy in Figure 13. Below the solvus temperature, the high volume fraction of γ' present in the microstructure pins the grain boundaries preventing recrystallization from occurring. [1,2] When recrystallization is prevented, residual strain is maintained in structure as shown in Figure 13d. In the case of a heat treatment with adequate temperature/time to allow for dissolution of γ' the pinning force is decreased, and recrystallization is able to occur. [43] For this reason, there is a strong correlation between a homogenous precipitate structure and a recrystallized grain structure, as shown previously in Figures 3, 5, 8, 10, and 12.

4.1.3. Grain Growth

One of the major findings of this work is the lack of rapid grain growth in the supersolvus condition outlined in Figure 10. Wrought Rene65 is processed in the subsolvus condition due to rapid grain growth which has deleterious effects on mechanical behavior. [43] The rapid grain growth in the wrought alloy is not found to occur in AM'ed Rene65. As illustrated in Figure 10, the grain size increased only marginally from 40.54 μm after 1 hour hold to 46.41 μm after 8 hour hold at 1150°C. For comparison, wrought Rene 65 begins coarsening at 1106°C (just below solvus) and shows significant grain growth at 1117°C (just above solvus). [36] Another independent study showed a 350% grain size increase within 1 hour at

1150°C for wrought Rene 65. [44] This feature of AM'ed Rene 65 can potentially expand the heat treatment window for the alloy and allow for more control over precipitate size and distribution.

The lack of grain growth is hypothesized to be caused by the following two factors. First, pinning is evidenced by tortuous grain boundaries shown in Figures 2d, 4c-d, 7 and 9c. This can be indicative of some segments of the grain boundaries being pinned while other segments continue to advance. As described previously, γ' precipitates that formed during heating completely dissolved during the supersolvus hold and would not pin the recrystallized grains at this temperature. It is common that very fine oxides or carbides can exist in the AM'ed microstructure that are too small to be detected in SEM. However, these oxides or carbides that cannot be detected by SEM, if present, would be below the typical length scale for conventional Zener pinning mechanism. [45] Nevertheless, if the oxides or carbides are the primary source for pinning force, they would exist in such a low volume that would allow for recrystallization to occur while preventing subsequent grain growth. The nature of the pinning by oxides or carbides is presently the subject of more detailed TEM investigation. Second, the lack of grain growth may result from a lack of driving force. Much of the strain energy present in the as-built condition is reduced by recrystallization in the supersolvus condition as seen in Figure 13 which may lead to a reduced driving force for grain growth. . In the literature, the effect of strain energy on grain growth of wrought Rene65 is not extensively studied. Hence, a future comparison study of between wrought versus AM'ed material is needed to understand the role of the strain energy on grain growth.

Grain growth and recrystallization behavior are shown schematically in Figure 18. With sufficient temperature and time, recrystallization occurs during solutionizing, as shown by the inset image 1b in this figure. Without sufficient temperature and time, no recrystallization occurs, and the directionally solidified microstructure is maintained due to precipitate pinning (as shown by 1a). There is no effect of hold time on grain size at supersolvus as previously discussed. Due to rapid reprecipitation in the case of supersolvus and retained precipitates in the case of subsolvus, no additional changes are seen to grain structure during cooling. Aging occurs well below the solvus temperature and therefore has no effect on the grain structure as well (as shown by 2).

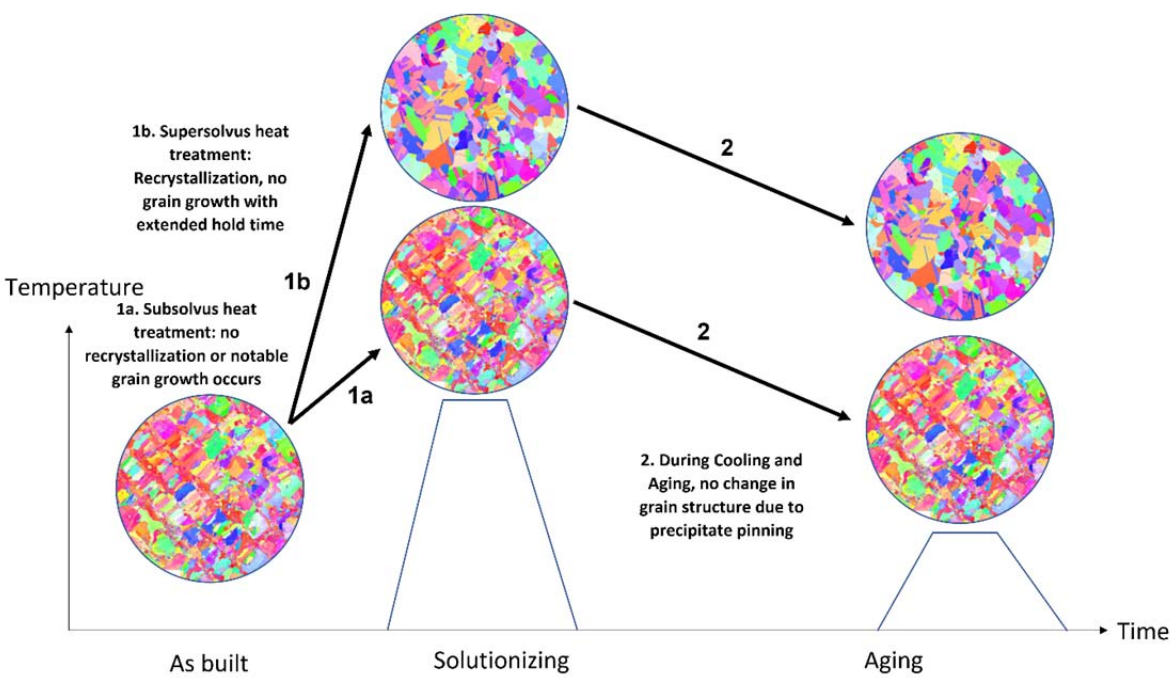

Figure 18: Schematic plot showing grain structure development through heat treatment process

4.2 Mechanical Behavior

4.2.1 Hot Tension and Loading Direction

Being a precipitation strengthened alloy, Rene65 derives much of its strength from precipitates. [46] It is designed as a fine-grained material and derives additional strength from grain boundary area. As shown in Figure 14, the lowest UTS and yield strength are seen in the as-built condition in both loading directions. This is due to the lack of precipitates present in the as-built condition prior to testing. Moreover, not enough time is spent at elevated temperature during hot tensile testing to develop the precipitation structure. The lower yield strength and UTS of heat-treated AM compared to wrought (Figure 14) is likely due to a larger grain size (e.g., wrought about 10 μm versus AM'ed about 40 μm). In other words, the decrease in grain boundary area with the increased grain size leads to the decreased tensile strength in AM'ed Rene65. [47,48]

Despite similar strength, there is reduced elongation to failure when loading transverse to the build direction. One possible explanation for this behavior is aligned defects formed during the printing process. [9] There is minimal to no visible cracking in the microstructure prior to testing in the samples observed in microscopes. However, there is still a possibility of microcracks or pores being present in the microstructure due to low sample size observed compared to total build height. Defects aligned along the build direction become planar defects when loading transverse to the build direction, causing loss of ductility in the material.

4.2.2 Tension Creep

As shown in Table IV, all tension creep tests were performed parallel to the build direction. As the defects from printing are expected to have a minimal effect on creep in the parallel direction, these tests would show the effect of microstructure on creep.

As shown in Figure 15, among the four conditions tested, the supersolvus heat treated AM'ed Rene65 has the longest life, exhibiting superior performance to the wrought material. The microstructural factors that are likely responsible for this improvement are summarized as follows. The first factor is an increase in average grain size. Specifically, the average grain size of the AM'ed supersolvus sample is 40.54 μm while the tested wrought grain size is on the order of 10 μm. Increased grain size can improve creep behavior as it decreases grain boundary assisted creep processes and reduces dislocation movement along the grain boundaries. [49] Grain boundary tortuosity, as previously shown to be present in the supersolvus microstructure seen in Figure 7 and 9c, can also improve creep behavior by limiting grain boundary sliding. [50] The second factor is a difference in precipitate size and precipitate distribution. As previously mentioned, in order to avoid rapid grain growth in the supersolvus regime, the wrought material undergoes a subsolvus heat treatment. This leads to a multimodal precipitate distribution with coarse primary γ' and fine secondary and tertiary γ' particles. On the other hand, supersolvus AM'ed material had finer homogenous γ' particles, as shown in Figure 4c and d.

To further examine the relative importance of the above two microstructure factors on creep, another interesting comparison can be made in the data for subsolvus AM'ed sample versus wrought sample (Figure 15). Both conditions resulted in similar coarse bimodal precipitate structure as both underwent the same heat treatment schedule. The main microstructure difference between the two is the grain structure. Specifically, as shown in Figure 5, the subsolvus samples show long columnar grains parallel to the build direction while varied grain sizes are seen transverse to the build direction. This can have an impact on the effective grain size; for example, for subsolvus at 1066°C, the grain size transverse to the build direction ranges 25-40 μm compared to grain size ranging from 40-80 μm parallel to the build direction.

The subsolvus AM’ed sample has an effective grain size that is much larger than the wrought sample, which is expected to be beneficial for creep. Hence, the fact that subsolvus AM’ed sample underperformed in creep than the wrought sample indicates that the larger grains in AM’ed samples did not likely have a predominant role on creep behavior. Instead, fine homogenous precipitate structures seem to be crucial to creep performance of AM’ed material. Effect of γ' precipitate distribution (e.g., size and spacing) on dislocation motion at elevated temperature is complex [51,52], and further study thus is necessary to better understand the mechanism for superior creep strength due to fine homogenous over bimodal precipitate structures in AM’ed material.

A final comparison can be made in the data for subsolvus AM’ed sample versus as-built sample with the latter outperforming the former in tension creep. Similar grain structure is seen between the as-built material and the subsolvus heat treated condition, as shown in Figures 1 and 5, respectively. Hence, what makes this comparison interesting is that the as-built microstructure does not contain discernable precipitate structure while the subsolvus AM’ed sample contains a coarse bimodal precipitate structure. The potential microstructural factors responsible for improved creep in as-built over subsolvus conditions are discussed as follows. First, the as-built microstructure contains a dislocation cell structure with high dislocation density, which has often been attributed to improved mechanical properties in the literature. [5,52] As shown in Figure 13, despite precipitates pinning grain boundary motion during subsolvus heat treatment, there is a small but noticeable amount of dislocation reduction, which likely has a negative effect on creep behavior. Second, while there are no discernable precipitates in the as-built condition, γ’ precipitates likely formed in-situ during the early stages of testing, which had a beneficial effect on creep similar to the fine homogenous precipitates in the supersolvus condition.

Figure 19 is a SEM image of as-built sample after creep testing. This microstructure contains a high fraction of small dark particles which are expected to be γ’precipitates formed in-situ during testing.

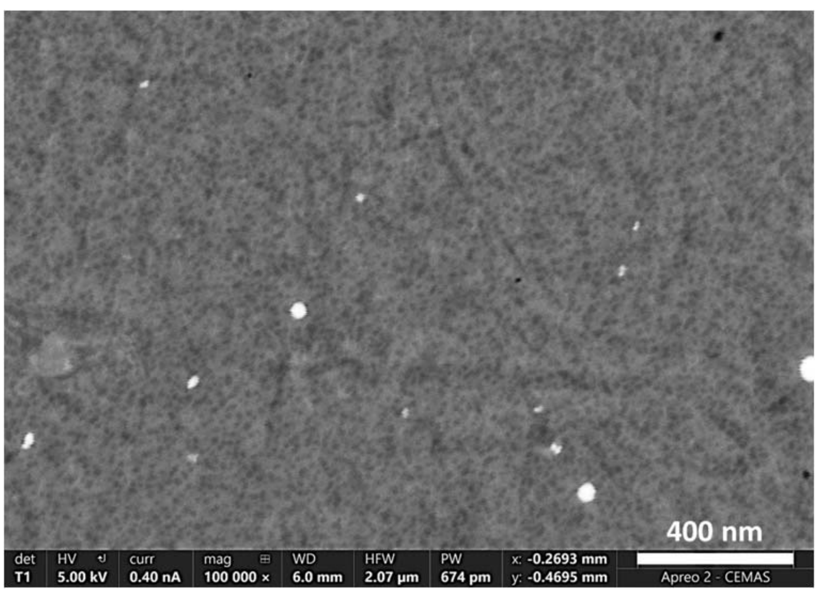

Figure 19: SEM image of post-creep-test as-built sample where fine dark particles are expected to be γ’ precipitates formed in-situ during testing

However, unlike the supersolvus condition, the precipitates formed in-situ during creep testing (see figure 19) are likely “under-developed” and their beneficial effect is thus limited. It is noted that such precipitate strengthening effect was not observed during the hot tension testing of as-built sample since there was insufficient time for precipitates to form.

4.2.3 Compression Creep

As shown in Figure 16, the recrystallized equiaxed microstructure with fine homogenous precipitates generally demonstrates superior compression creep behavior, a trend consistent with that in tension creep described in the previous section. However, this is not always the case. Longer hold times near solvus (1100°C), despite allowing for recrystallization, is detrimental to compression creep behavior. A similar detriment to creep behavior is observed with increased hold times at supersolvus (1150°C). There is no obvious difference in grain size, grain structure, precipitate size, or precipitate distribution due to hold time, as shown in Figures 6 through 8 for near solvus (1100°C) and in Figures 9 and 10 for supersolvus (1150°C).

Two hypotheses are described below for the detrimental effect of extended hold time on creep behavior. The first is the growth of brittle oxide particles. There is some evidence in the literature that nanoscale oxides are present in the as-built microstructure. [45,54,55] With extended hold times at 1066°C and 1150°C these oxides are likely to coarsen. These large brittle particles particularly when they are aligned can greatly impact ductility and lead to failure at lower strain. [55,56] The second is the homogenization of boron. Rene65 contains a small amount of boron which is added to improve creep behavior in the form of discrete boride particles along the grain boundaries. For example, boride particles of approximately 1 μm in size have been observed to locate preferentially on grain boundaries in wrought Rene65. [58] During printing, the rapid cooling may result in boron segregation into the inter-dendritic regions. The fine dendrite arm spacing in the AM'ed material may decrease the homogenization time. [57] The literature has shown that the back diffusion of boron away from the grain boundaries to the grain interior can occur during heat treatment of some materials. [58] Hence, it is possible that extended hold time at the supersolvus temperature aids in boron homogenization, resulting in a decrease of boron content around the grain boundaries and subsequently a reduced creep property. The heat-treated AM'ed microstructure comprises nano-scale secondary particles (which can include borides) that were uniformly dispersed with no clear preferential nucleation between grain boundaries and grain interiors, which is in stark contrast to wrought microstructure with micro-scale borides along grain boundaries. Future characterization in TEM is needed to determine the mechanism(s) for the detrimental effect of extended supersolvus hold time on creep behavior. Although compression creep test is expected to be less sensitive to printing defects than tensile creep test, the small sample size (i.e., 7mm×2.8mm×2.8 mm) may introduce variability in the observed creep results. In particular, Figure 16 shows that among the three samples supersolvus-solutioned at 1150°C and then tested perpendicular to the build direction (designated by the three circles), the sample with slow cooling and bimodal precipitate structure significantly outperformed the two samples with fast cooling and uniform precipitate structure. Such superior performance of bimodal precipitate structure is unexpected and could be caused by the small specimen happening to sample a region containing few defects and brittle oxides.

4.2.4 Anisotropy in Tension Versus Compression Creep

There is a distinct anisotropy in the creep behavior for tension loading versus compression loading. In the literature, this has been attributed to the development of defects and cracks over the course of testing. Specifically, the primary difference between compression and tension creep is thought to occur in the tertiary creep stage where cavitation, void formation and cracking take place. In tension these defects will be opened further leading to continued decrease of the effective cross section. In the case of compression, these defects will be "closed" and are less likely to continue to decrease the cross-sectional area. In cases where defects are already present, which may be the case in many additively manufactured parts include the Rene65 studied here, the tertiary creep stage is initiated more rapidly and a larger anisotropy between tension and compression is observed. There is also seen to be variations in deformation modes between tension and compression creep such as twinning. [59-62]

5. Summary and Conclusions

In summary, an extensive set of microstructure and mechanical property data for Rene65, a medium γ' nickel superalloy printed by powder bed fusion-laser additive manufacturing, is reported in this study. The results show that the standard heat treatments developed for traditional cast or wrought alloys need to be modified for additively manufactured materials to utilize their unique microstructure for sound mechanical properties. The specific conclusions are as follows:

The solutionizing heat treatment temperature and cooling rate had a large effect on the grain and precipitate structures. For subsolvus or near solvus and short hold time, no recrystallization took place, and the as-built grain structure was maintained with a bimodal precipitate structure for either slow or fast cooling rate. For supersolvus heat treatment or near solvus and long hold time, equiaxed grain structure formed, greatly reducing the dislocation content in the as-built structure. Moreover, the fast cooling rate resulted in fine γ' precipitates while the slow cooling rate formed bimodal distribution of γ' precipitates. These results indicate that γ' precipitates can rapidly form during the heating portion of the solutionizing heat treatment and can pin the grain boundary if not dissolved at the solutionizing temperature.

Additively manufactured Rene65 can be supersolvus heat treated without the detrimental effects seen in the cast/wrought alloy. This is due to a notable lack of rapid grain growth seen in the additively manufactured material. Possible factors for the lack of grain growth include nanoscale oxide or carbide particles pinning the grain boundary as well as a lower driving force for grain growth compared to the wrought material. However, supersolvus hold time needs to be carefully controlled as extended hold time can significantly degrade the creep property, a behavior hypothesized to be caused by excess coarsening of oxides and homogenization of boron for long hold time.

The as-built alloy behaved better in creep than the additively manufactured alloy that was subjected to subsolvus heat treatment, which is the standard method for traditional cast or wrought alloy. This has been attributed to strengthening based on the dislocation cell structure and rapid precipitation during testing. The supersolvus heat treated material outperformed the wrought material in creep, which has been attributed to a finer homogenous precipitate structure in the former.

Finally, the additively manufactured alloy exhibited large anisotropy in the hot tension behavior with respect to the parallel versus transverse loading direction and in the creep behavior with respect to tension versus compression loading. This has been primarily attributed to existence of defects in the additively manufactured alloy. Future work involving hot isostatic pressing will be used to better understand the effect of defects on mechanical behaviors.

Acknowledgements

The authors wish to acknowledge the financial support from the U.S. National Science Foundation NSF I/UCRC Manufacturing and Materials Joining Innovation Center (Ma2JIC) under Grant No. 1822144.

Conflict of Interest

On behalf of all authors, the corresponding author states that there is no conflict of interest.

References

[1] C.M. Katsari, S. Katnagallu, and S. Yue: Materials Characterization, 2020, vol. 169, p. 110542.

[2] J. Heaney, M. Lasonde, A. Powell, B. Bond, C. O'Brien: 8th International Symposium on Superalloy 718 and Derivatives, 2014, pp. 67-77.

[3] ISO/ASTM: 52900:2021 €.

[4] M. Cheng, X. Xiao, G. Luo, L. Song: Optics and Laser Technology, 2021, vol. 142, p. 107137.

[5] H.E. Sabzi, N.T. Aboulkhair, X. Liang, X.H. Li, M. Simonelli, H. Fu, and P.E.J. Rivera-Diaz-del-Castillo: Materials and Design, 2020, vol. 196, p. 109181.

[6] S.H. Sun, K. Hagihara, and T. Nakano: Materials and Design, 2018, vol. 140, pp. 307-316.

[7] T. Ishimoto, K. Hagihara, K. Hisamoto, S.H. Sun, and T. Nakano: Scripta Materialia, 2017, vol. 132, pp. 34-38.

[8] P. Karimi, E. Sadeghi, J. Algardh, A. Kedhavarzkermani, R. Esmaeilizadeh, E. Toyserkani, and J. Andersson: Additive Manufacturing, 2021, vol. 46, p. 102086.

[9] E. Hosseini, and V.A. Popovich: Additive Manufacturing, 2019, Vol. 30, p. 100877.

[10] Y.L. Kuo, S. Horikawa, and K. Kakehi: Scripta Materialia, 2017, vol. 129, pp. 74-78.

[11] Y.L. Kuo, A. Kamigaichi, and K. Kakehi: Metallurgical and Materials Transactions A: Physical Metallurgy and Materials Science, 2018, vol. 49, pp. 3831-3837.

[12] T.D. McLouth, D.B. Witkin, G.E. Bean, S.D. Sitzman, P.M. Adams, J.R. Lohser, J.M. Yang, and R.J. Zaldivar: Materials Science and Engineering A, 2020, vol. 780, p. 139184.

[13] A.C. Hautfenne, S. Nardone, E. de Bruycker, and C. Hautfenne: 4th international ECCC conference, 2017, p. 321267580.

[14] S. Pratheesh Kumar, S. Elangovan, R. Mohanraj, and J.R. Ramakrishna: Materials Today: Proceedings, 2021, vol. 46, pp. 7892-7906.

[15] M. Probstle, S. Neumeier, J. Hopfenmuller, L.P. Freund, T. Niendorf, D. Schwarze, and M. Goken: Materials Science and Engineering A, 2016, vol. 674, pp. 299-307.

[16] B. Rogers, A. Tasooji, B. Rogers, and W. Petuskey: thesis presentation, Arizona State University, 2017.

[17] B. Shassere, D. Greeley, A. Okello, M. Kirka, P. Nandwana, and R. Dehoff: Metallurgical and Materials Transactions A: Physical Metallurgy and Materials Science, 2018, vol. 49, pp. 5107-5117.

[18] L.Y. Wang, Y.C. Wang, Z.J. Zhou, H.Y. Wan, C.P. Li, G.F. Chen, and G.P. Zhang: Materials and Design, 2020, vol. 195, p. 109042.

[19] D.B. Witkin, R.W. Hayes, T.D. McLouth, and G.E. Bean: Metallurgical and Materials Transactions A: Physical Metallurgy and Materials Science, 2019, vol. 50, pp. 3458-3465.

[20] Z. Xu, C.J. Hyde, A. Thompson, R.K. Leach, I. Maskery, C. Tuck, A.T. Clare: Materials and Design, 2017, vol. 133, pp. 520-527.

[21] Z. Xu, C.J. Hyde, C. Tuck, and A.T Clare: Journal of Materials Processing Technology, 2018, vol. 256, pp. 13-24.

[22] Z. Xu, J.W. Murray, C.J. Hyde, and A.T. Clare: Additive Manufacturing, 2018, vol. 24, pp. 486-497.

[23] A. Kreitcberg, K. Inaekyan, S. Turenne, and V. Brailovski: Journal of Manufacturing and Materials Processing, 2019, vol. 3, p. 75.

[24] K.T. Son, T.Q. Phan, L.E. Levine, K.S. Kim, K.A. Lee, M. Ahlfors, and M.E. Kassner: Materialia, 2021, vol. 12, p. 101021.

[25] P. Fernandez-Zelaia, Y. Lee, S. Dryepondt, and M.M. Kirka: International Journal of Plasticity, 2022, vol. 151, p. 103177.

[26] J. Xu, H. Gruber, D. Deng, R.L. Peng, and J.J. Moverare: Acta Materialia, vol. 179, pp. 142-157.

[27] N.S. Moghaddam, S. Saedi, A. Amerinatanzi, A. Hinojos, A. Ramanzi, J. Kundin, M.J. Mills, H. Karaca, M. Elahinia: Nature Scientific Reports, 2019, Vol 9(41), p. 30631084.

[28] S. Lampman: Weld integrity and performance, ASM International, Materials Park, OH, 1997, pp. 3-5.

[29] M. Haines, V.V. Rielli, S. Primig, N. Haghdadi: Journal of Material Science, 2022, vol 57, pp. 14135-14187.

[31] I. Gutierrez-Urrutia, F. Archie, D. Raabe, F. Yan, N. Tao, K. Lu: Science and Technology of Advanced Materials, 2016, Vol.17(1), pp. 29-36.

[31] S.L. Semiatin, D.W. Mahaffey, N.C. Levkulich, O.N. Senkov, and J.S. Tiley: Metallurgical and Materials Transactions A: Physical Metallurgy and Materials Science, 2018, vol. 48, pp. 6265-6276.

[32] T. Grosdidier, A. Hazotte, and A. Simon: Scripta Metallurgica et Materialia, 1994, vol. 30, pp. 1257-1262.

[33] C.M. Katsari: thesis presentation, Mcgill University, 2021.

[34] G. Muralidharan, and H. Chen: Science and Technology of Advanced Materials, 2000, vol. 1, pp. 51-62.

[35] C. Papadaki, W. Li, and A.M. Korsunsky: Materials, 2018, vol. 11, p. 1528.

[36] A. Wessman, Dissertation, University of Cincinnati, 2016.

[37] M. Yang, L. Wang, and W. Yan: Npj Computational Materials, 2021, vol. 7, p. 56.

[38] N. Sargent, M. Jones, R. Otis, A.A. Shapiro, J.P. Delplanque, and W. Xiong: Metals, 2021, vol. 11(4), p. 570.

[39] H. Liu, Z. Cheng, W. Yu, Q. Cai: Materials Research Express, 2021, Vol. 8, p. 046539.

[40] N. Mavrikakis, P.R. Calvillo, W. Saikaly, M. Descoins, D. Mangelinck, M. Dumont: IOP Conf. Series: Materials Science and Engineering, 2018, p. 012016.

[41] C. Slater, A. Mandal, C. Davis: Metallurgical and Materials Transactions B, 2019, Vol. 50B, pp. 1627-1636.

[42] Y. Cao, P. Bai, F. Liu, X. Hou, and Y. Guo: Materials, 2020, vol. 13, p. 340.

[43] K. Alvarado, I. Janeiro, S. Florez, B. Flipon, J.M. Frachet, D. Locq, C. Dumont, N. Bozzolo, and M. Bernacki: Metals, 2021, vol. 11, p. 1921.

[44] M.A. Charpagne, Unpublished Work, University of Illinois, 2021.

[45] F. Yan, W. Xiong, E. Faierson, G.B. Olson: Scripta Materialia, 2018, vol. 155, pp. 104-108.

[46] E.I. Galindo-Nava, L.D. Connor, C.M.F. Rae: Acta Materialia, 2015, vol. 98, pp. 377-390.

[47] G. Malakondaiah, and P.R. Rao: Def Sci J, 1985, vol. 35, pp. 201-217.

[48] H. Zhang, Z. Xu, L.J. Kecskes, S. Yarmolenko, and J. Sankar: Crystals, 2021, vol. 11(10), p. 1128.

[49] R. Raj, and M.F. Ashby: Metallurgical Transactions, 1971, vol. 2, pp. 1113-1127.

[50] M.A. Ali, I. Lopez-Galilea, S. Gao, B. Ruttert, W. Amin, O. Shchyglo, A. Hartmaier, W. Theisen, and I. Steinbach: Materialia, 2020, vol. 12, p. 100692.

[51] D. Seidman, E. Marquis, D. Dunand: Acta Materialia, 2002, vol. 50, pp. 4021–4035.

[52] T. Gallmeyer, S. Moorthy, B. Kappes, M. Mills, B. Amin-Ahmadi, A. Stebner: Additive Manufacturing, 2020, Vol. 31, p. 100977.

[53] P. Deng, M. Song, J. Yang, Q. Pan, S. McAllister, L. Li, B. Prorok, X. Lou: Material Science and Engineering A, 2022, vol. 835, p. 142690.

[54] X. Zhang, H. Cao, X. Yang, Y. Zhao, H. Wang, X. Mao, Y. Zhai: Fusion Engineering and Design, 2021, vol. 164, p. 112213.

[55] O. Adegoke, J. Andersson, H. Brodin, R. Pederson: Metals, 2022, vol. 10(8), p. 996.

[56] J. Campbell: Complete Casting, 2nd Edition, Butterworth-Heinemann, Oxford, UK, 2015, pp. 821-882.

[57] X.L. He, Y.Y. Chu, J.J. Jonas: Acta Metallurgica, 1989, Vol. 37(11), pp. 2905-2916.

[59] T. Wojcik, M. Rath, E. Kozeschnik: Materials and Technology, 2018, Vol. 24(13) pp. 1558-1564.

[59] G.P. Tilly, and G.F. Harrison: Journal of strain analysis, 1972, vol. 7(3), pp. 163-169.

[60] H. Wang, Q.D. Wang, C.J. Boehlert, D.D. Yin, and J. Yuan: Materials Characterization, 2015, vol. 99, pp. 25-37.

[61] K. Kakehi: Scripta Materialia, 1999, Vol. 41, pp. 461-465.

[62] N. Tsuno, S. Shimabayashi, K. Kakehi, C.M.F. Rae, and R.C. Reed: 11th international symposium on superalloys, TMS, 2008, pp. 433-442.